Activating Sodium Intercalation in Cation-Deficient Fe$_3$O$_4$ Through Mo Substitution

Shasha Guo, Mohamed Ait Tamerd,* Changyuan Li, Xinyue Shi, Menghao Yang, Jingrong Hou, Jie Liu, Mingxue Tang, Shu-Chih Haw, Chien-Te Chen, Ting-Shan Chan, Chang-Yang Kuo, Zhiwei Hu, Long Yang,* and Jiwei Ma*

Magnetite (Fe$_3$O$_4$), a conversion-type anode material, possesses high capacity, cost-effectiveness and environmental friendliness, positioning it as a promising candidate for the large-scale energy storage applications. However, the multi-electron reactions in sodium-ion batteries face challenges originated from the electrochemical inactivity of Na$^+$ intercalation in the conversion-type oxides. In this work, controllable Fe vacancies are tailored in Fe$_3$O$_4$ lattice through the gradient Mo doping. The pair distribution function local structure analysis reveals that the key to stabilizing more Fe vacancies lies in the uniform occupation of Mo dopants at both tetrahedral (8a) and octahedral (16d) sites. The vacancy-rich structure, featuring 7.3% Fe vacancies, achieves a significantly enhanced capacity of 127 mAh g^{-1} after 150 cycles at 100 mA g^{-1}, in comparison with the 37 mAh g^{-1} for defect-free Fe$_3$O$_4$. A comprehensive understanding of how the defective structure relates to electrochemical performance is presented, combining physical-electrochemical characterizations with theoretical calculations. The occurred Mo-O interactions enhances electronic conductivity and diminishes electrostatic interactions between intercalated Na$^+$ and lattice O^{2-}. Concurrently, Fe vacancies facilitate bulk Na$^+$ migration with lower energy barrier. This study presents a prospect for modulating the defective structure in transition metal oxides to activate fast and reversible sodium intercalation toward high-performance sodium-ion batteries.

1. Introduction

The success of lithium-ion batteries (LIBs) has pushed the fast development of electrical energy storage systems, which is pivotal for electric vehicles and grid storage applications.[1] Despite the promising prospects, the limited and unevenly distributed resources of lithium pose a significant challenge in meeting the increasing demands of mass production of LIBs.[2] Therefore, identifying alternative energy systems based on the earth-abundant elements for large-scale applications that align with sustainability is of vital importance. In this context, sodium-ion batteries (SIBs) present a compelling alternative thanks to the similar chemistries of Na and Li, coupled with the abundance of Na resources and the non-toxicity.[3] Despite having the same cell configurations, the various intrinsic properties of Na$^+$ compared with Li$^+$, such as the larger ionic radius, lower redox potential, and higher electrochemical activity, result in a lower energy density for SIBs comparing with LIBs.[2c,4] Thus, developing high-performance electrodes materials for SIBs that combine high capacity and adequate potential for large-scale applications remains a challenge.

Extensive research has been conducted to identify active electrode materials for SIBs, based on the foundations laid by LIBs.[5] For cathode materials, layered sodium transition-metal oxides, polyanionic compounds, and/or Prussian blue analogs have demonstrated considerable potential in terms of working voltage and capacity.[6] However,

S. Guo, M. Ait Tamerd, C. Li, X. Shi, M. Yang, J. Hou, L. Yang, J. Ma
Shanghai Key Laboratory for R&D and Application of Metallic Functional Materials
Institute of New Energy for Vehicles
School of Materials Science and Engineering
Tongji University
Shanghai 201804, China
E-mail: ait_tamerd_mohamed@tongji.edu.cn; long_yang@tongji.edu.cn; jiwei.ma@tongji.edu.cn
J. Liu, M. Tang
Center for High Pressure Science & Technology Advanced Research
Beijing 100094, China

S.-C. Haw, C.-T. Chen, T.-S. Chan, C.-Y. Kuo
National Synchrotron Radiation Research Center
101 Hsin-Ann Road, Hsinchu 300092, Taiwan
C.-Y. Kuo
Department of Electrophysics
National Yang Ming Chiao Tung University
Hsinchu 300093, Taiwan
Z. Hu
Max Planck Institute for Chemical Physics of Solids
Nöthnitzer Strasse 40, 01187 Dresden, Germany

**ADVANCED
SCIENCE NEWS**

www.advancedsciencenews.com

**NANO · MICRO
small**

www.small-journal.com

their capacity improvement is restricted by the initially limited intercalation sites.[7] For anode materials, graphite, most widely used in commercial LIBs, faces challenges in SIBs due to the hindrance of Na^+ intercalation by Na-ion plating.[8] Consequently, non-graphitic hard carbon has been explored, showing promising desodation capacity for SIBs.[9] Nonetheless, the underlying mechanisms related to the Na^+ storage and Na dendrites in hard carbon anodes require further investigation.[10] Compared with the carbonaceous-based anodes, transition metal oxides (TMOs) are promising candidates due to their high capacity derived from multielectron transfer and their diverse structures facilitating the design of targeted materials.[11] Notably, Magnetite (Fe_3O_4), with its inverse-spinel structure, offers sufficient interstitial sites and a three-dimensional network for metal ion storage. Thanks to the multi-valence of Fe^{2+}/Fe^{3+} ions, an 8-electron transfer reaction occurs during the sodiation, exhibiting a theoretical capacity of up to 926 mAh g^{-1}.[12] Moreover, the eco-friendliness and cost-effectiveness of Fe_3O_4 make it an economically viable material for large-scale applications. However, the electrochemical performance of Fe_3O_4 anode in SIBs is restricted by the large radius of Na^+ compared with Li^+, causing sluggish kinetics and limited capacity, which is responsible for the electrochemically inactive versus Na intercalation.[2c,13]

To address above-mentioned issues, strategies including nanostructuring combined with various carbon matrices, optimizing process conditions, and enhancing extrinsic features have been used.[14] In the meantime, cationic defects have garnered much attention in regulating intrinsic atomic and electronic structures of Fe_3O_4 to achieve a considerably high performance toward Li intercalation.[15] During the intercalation process, cationic vacancies serve as active sites that not only create lower-energy migration paths for fast metal ion intercalation, but also influence the charge storage process, thereby significantly improving the cycling stability and rate capability.[16] In our previous work, only 1.7% Fe vacancies was stabilized via a limited amount of Mo^{4+} dopant, significantly improving the Li intercalation.[17] Here, we further increase the content of Mo^{4+} dopants from 5% to 20% in order to generate more Fe vacancies. The pair distribution function (PDF) analysis reveals that the key to stabilize more Fe vacancies lies in the uniform occupation of Mo atoms at both the tetrahedral (8a) and octahedral (16d) sites rather than exclusively locating at 16d sites in low-content 5.3% Mo-doped compound. Electrochemical characterizations demonstrate that the presence of Fe vacancies could activate the reversible Na^+ intercalation into Fe_3O_4, yielding the improved capacity and Na^+ diffusion kinetics. Mechanistic insights from operando and ex situ X-ray diffraction (XRD), synchrotron X-ray absorption spectroscopy (XAS) and density functional theory (DFT) calculations suggest that Fe vacancies provide favorable ion intercalation sites and accelerate diffusion through the lower-energy "vacancy-mediated" migration path, activating the reversible and fast Na^+ storage.

2. Results

2.1. Physicochemical Characterizations

The physicochemical structure of the series Mo-substituted Fe_3O_4 samples denoted as $Fe_{3-4x/3}\square_{x/3}Mo_xO_4$ (where x = 0.00,

0.05, 0.10, 0.15, 0.20, and $\square$ represents Fe vacancies), are first identified using powder XRD. XRD patterns are all well indexed to the single-phase Fe_3O_4 structure (PDF No. 04-005-4319), confirming successful Mo substitution within appropriate molar ratios of Mo dopants (≤20 at.%) (Figure S1, Supporting Information). Nevertheless, at a Mo doping ratio of 25 at.%, unexpected peaks attributed to the FeO phase (PDF No. 04-001-9939) emerge.[17] To further elucidate the atomic structure, PDF analysis based on the high-energy synchrotron x-ray total scattering data is performed, as shown in **Figure 1a** and **Table 1**, allowing the identification of atomic pairs of distance r apart at the subnanometer length scale.[18] The initial structure model is an inverse-spinel configuration, $[Fe^{3+}]_{8a\text{-}tetra}[Fe^{2+}Fe^{3+}]_{16d\text{-}octa}O_4$, with half of Fe^{3+} ions occupying tetrahedral 8a sites, the other Fe^{3+} and Fe^{2+} ions at octahedral 16d sites. The suitability of the chosen model is validated by the satisfactory fitting of the un-doped Fe_3O_4 sample. For the Mo-doped samples, Mo dopants are initially presumed to occupy octahedral 16d sites, referring to our previous extended X-ray absorption fine structure (EX-AFS) analysis and DFT calculations.[17] The Mo/Fe ratio for the 5 at.% Mo-doped sample (x = 0.05) was consistent with our previous study. However, when Mo content increases from x = 0.10 to 0.20 with the 16d Mo occupying model, there is a large discrepancy of Mo/Fe ratios between the results obtained by PDF (Table S1, Supporting Information), energy-dispersive X-ray spectroscopy (EDS) (Figure S2, Supporting Information), and inductively coupled plasma-optical emission spectrometry (ICP-OES) (Table S2, Supporting Information). It is suggested that our presumption of Mo exclusively locating at octahedral 16d sites is inappropriate when the Mo content is >5 at.%. Consequently, a detailed PDF structural refinement was carried out, considering the co-occupancy of Mo at both 8a and 16d sites, with the corresponding structural information summarized in Table 1. Notably, this model indicates a similar distribution of Mo at both sites, while the charge-compensated Fe vacancies locate mostly at the 16d sites and increase with the increased Mo content, supported by XRD Rietveld refinements (Figure S1 and Table S3, Supporting Information). Indeed, the occupancy of Mo^{4+} is refined to be 5.3%, 11.1%, 16.5%, and 22.3% for the $Fe_{3-4x/3}\square_{x/3}Mo_xO_4$ (x = 0.05, 0.10, 0.15, 0.20) samples, respectively, yielding Fe^{3+} vacancies of 1.7%, 3.6%, 5.5%, and 7.5%. The chemical formula of Mo-doped compounds are determined to be $Fe_{2.93}\square_{0.017}Mo_{0.053}O_4$, $Fe_{2.853}\square_{0.036}Mo_{0.111}O_4$, $Fe_{2.780}\square_{0.055}Mo_{0.165}O_4$ and $Fe_{2.702}\square_{0.075}Mo_{0.223}O_4$ for x = 0.05, 0.10, 0.15 and 0.20, respectively.

The valence state of Mo is determined by the Mo L_3 edge XAS spectra,[19] as shown in Figure 1b. An increase in the valence state of 4d transition metal ion typically leads to an energy shift of the $L_{2,3}$ XAS spectra by one or more eV to higher energies.[20] The Mo L_3 spectra for $Fe_{3-4x/3}\square_{x/3}Mo_xO_4$ samples align with the energy position of MoO_2, indicating the Mo^{4+} valence state in $Fe_{3-4x/3}\square_{x/3}Mo_xO_4$ samples. However, differences in the detailed line shapes confirm the successful incorporation of Mo^{4+} ions into the Fe_3O_4 matrix rather than forming a MoO_2 phase. The Fe L_3 edge XAS spectra of $Fe_{3-4x/3}\square_{x/3}Mo_xO_4$ samples are presented in Figure 1c. The energy position and multiplet spectral feature at the 3d transition elements $L_{2,3}$ edge are highly sensitive to their valence state[21] and local environment.[22] The mixed valence of Fe ions can be inferred from the L_3 peak positions, which are
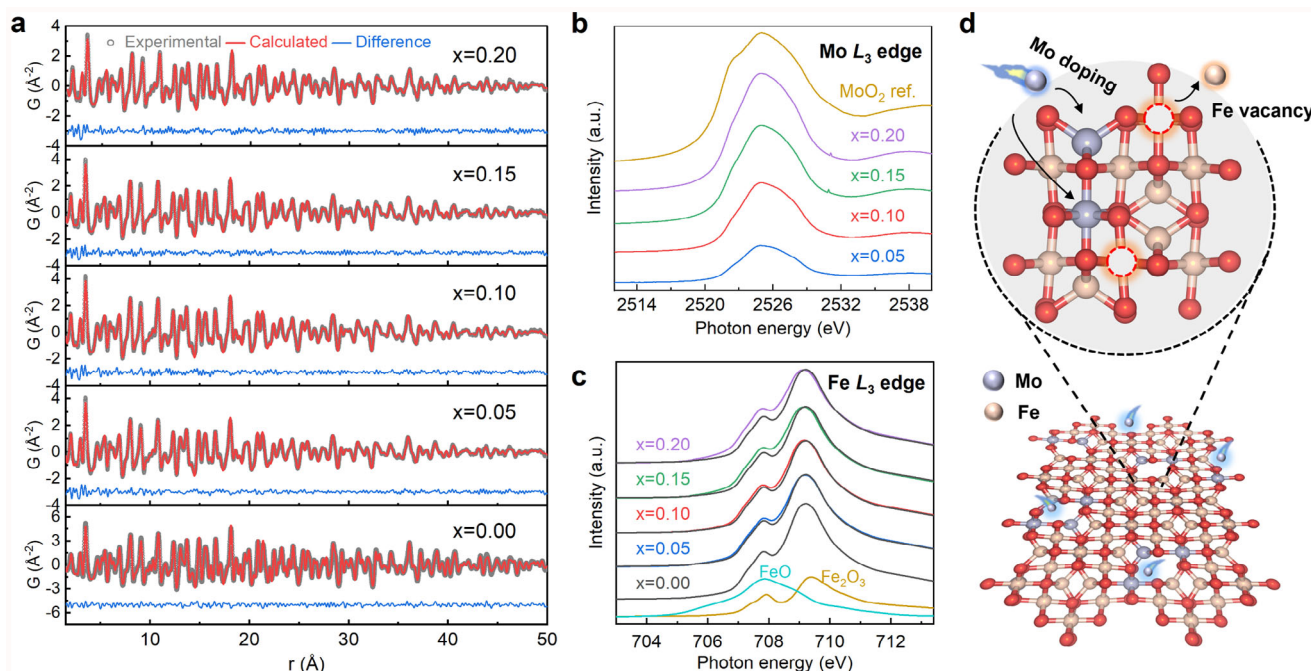
**ADVANCED
SCIENCE NEWS**

www.advancedsciencenews.com

**NANO · MICRO
small**

www.small-journal.com

Figure 1. Structural analysis of the as-prepared Mo-doped $Fe_{3-4x/3}\square_{x/3}Mo_xO_4$ ($x = 0.00, 0.05, 0.10, 0.15, 0.20$). a) The experimental x-ray PDF data (gray) are fit over the range of $1.5 < r < 50$ Å by the $Fe_{3-4x/3}\square_{x/3}Mo_xO_4$ ($x = 0.00, 0.05, 0.10, 0.15, 0.20$) phase model (red). The offset below is the difference curve (blue). b) Mo L_3 edge XAS spectra. c) Fe L_3 edge XAS spectra, in which the $x = 0.00$ and $x = 0.05$ samples are excerpted from the previous work.[17] d) Schematic representations of Mo doping and Fe vacancy structure.

located between FeO and Fe_2O_3 references.[23] Moreover, as the Mo dopant concentration increases from 0.05 to 0.20, the lower-energy peak becomes more pronounced, aligning with the divalent FeO reference. A detailed analysis of Fe valence state is conducted using a configuration interaction cluster model with reference spectra from bulk Fe_2O_3, FeO, and $YBaCo_3FeO_7$,[22a,24] serving as references for Fe^{3+} at the octahedron site (Fe_{octa}^{3+}), Fe^{2+} at the octahedron site (Fe_{octa}^{2+}) and Fe^{3+} at the tetrahedron site (Fe_{tetra}^{3+}), respectively. The simulations (Figure S3, Supporting Information) reveal that the ratio of Fe_{tetra}^{3+} remains constant,

while the proportion of Fe_{octa}^{3+} slightly decreases and the Fe_{octa}^{2+} increases with the increase of Mo dopants. This trend gives rise to a gradually reduced average oxidation state of the Fe species from 2.72 to 2.63.

High-resolution transmission electron microscopy (HR-TEM) and scan electron microscopy (SEM) coupled with EDS, reveal similar crystal microstructures and morphologies across the series of Mo-doped samples. **Figure 2** displays representative micrographs of 10–20 at.% Mo-doped samples, while images for 5 at.% Mo-doped and undoped Fe_3O_4 have been

Table 1. Crystallographic details of Mo-doped sample series $Fe_{3-4x/3}\square_{x/3}Mo_xO_4$ ($x = 0.00, 0.05, 0.10, 0.15, 0.20$) obtained from the x-ray PDF analysis. R_w is the goodness-of-fit parameter. U_{iso} (units of Å^2) is the isotropic atomic displacement parameter (ADP). Occupancy is the atomic percent of elements at the lattice sites.

Fitting range: 1.5–50 Å		$x = 0.00$	$x = 0.05$	$x = 0.10$	$x = 0.15$	$x = 0.20$
R_w		0.1365	0.1488	0.1512	0.1566	0.1488
U_{iso}	Fe1 (8a)	0.0047	0.0148	0.0094	0.0097	0.0090
	Fe2 (16d)	0.0085	0.0098	0.0150	0.0141	0.0140
	Mo1 (8a)			0.0101	0.0098	0.0092
	Mo2 (16d)		0.0198	0.0098	0.0145	0.0146
	O	0.0092	0.0203	0.0208	0.0206	0.0200
Occ.	Fe1 (8a)		1.1209	1.0176	0.9865	0.9676
	Fe2 (16d)		0.9210	0.9398	0.9298	0.9250
	Mo1 (8a)			0.0623	0.0830	0.0952
	Mo2 (16d)		0.0272	0.0242	0.0411	0.0637
Mo Occupancy			0.0544	0.1106	0.1652	0.2226
Mo/Fe (atomic ratio)			0.0184	0.0382	0.0581	0.0790

**ADVANCED
SCIENCE NEWS**
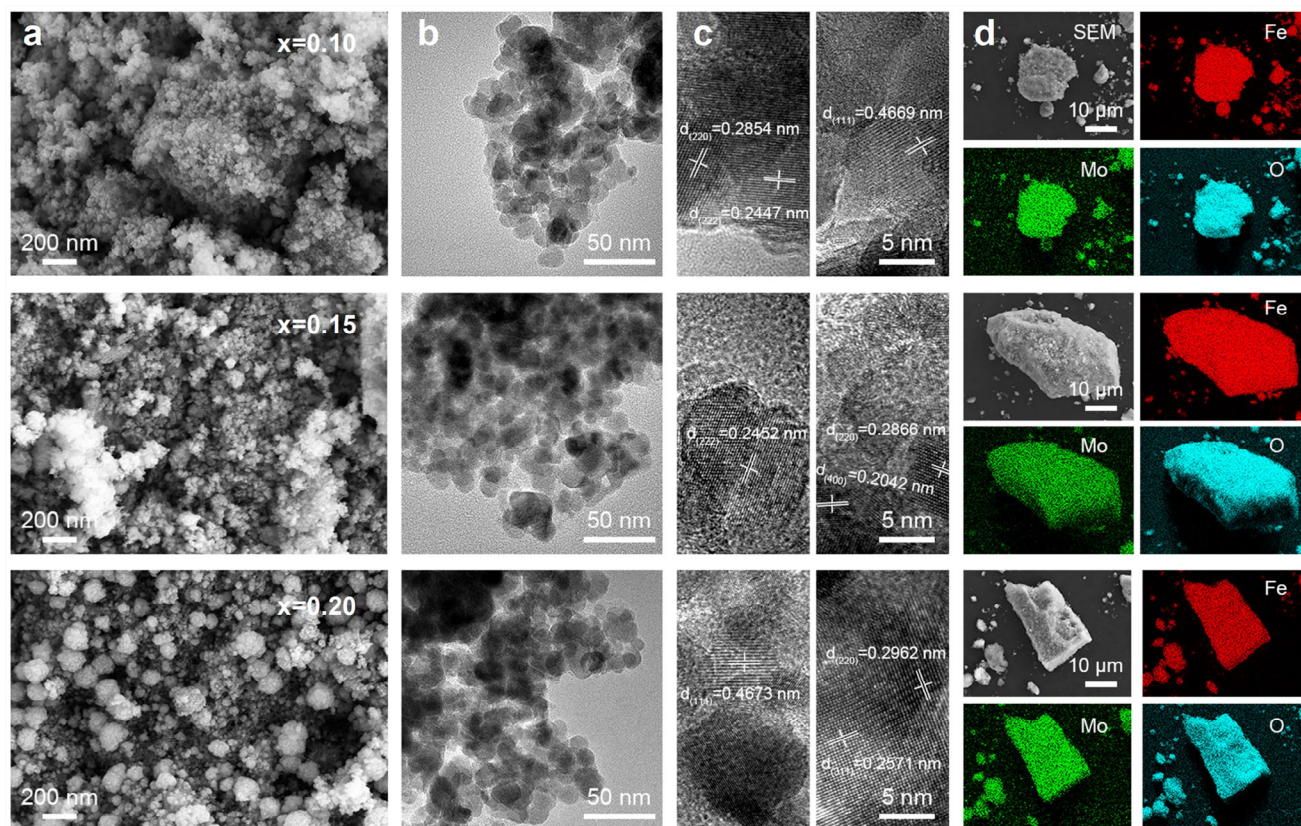www.advancedsciencenews.com

NANO · MICRO
small
www.small-journal.com

Figure 2. Morphology and microstructure characterizations for $Fe_{3-4x/3}\square_{x/3}Mo_xO_4$ (x = 0.10, 0.15, and 0.20) samples. a) SEM images in a scale bar of 200 nm; b) HR-TEM images in a scale bar of 50 nm; c) Representative interplanar spacings of the inversed spinel lattice, scale bar: 5 nm; d) EDS-SEM images and mappings of Mo, Fe, O atoms.

previously reported.[17] The SEM images in Figure 2a illustrate the nanoscale spherical particles with diameters of ≈20 nm. This nanosized structure is corroborated by HR-TEM images in Figure 2b, which also highlight the high crystallinity of particles through the distinct lattice fringes in Figure 2c. The typical lattice stripes with interplanar spacing measured at 0.2042, 0.2447, 0.2571, 0.2962 and 0.4669 nm, correspond to the (400), (222), (311), (220), and (111) facets of Fe_3O_4, respectively. Interestingly, an expansion of the lattice planes with increasing Mo dopant concentration is observed due to the higher ionic radius of Mo^{4+} than Fe^{3+} (0.79 Å vs 0.65 Å),[25] consistent with the larger lattice constants derived from XRD refinements. The enlarged lattice confirms that a limited amount of Mo dopants can effectively expand the cell, which is favorable for ion diffusion. Furthermore, the EDS surface scans from SEM in Figure 2d confirm a homogeneous distribution of Fe, Mo, and O atoms across the samples, justifying the successful substitution of Mo dopants.

2.2. Electrochemical Performance

The first galvanostatic discharge-charge profiles of $Fe_{3-4x/3}$-$\square_{x/3}Mo_xO_4$ (x = 0.00, 0.05, 0.10, 0.15 and 0.20, denoted as Fe_3O_4, 005Mo-, 010Mo-, 015Mo- and 020Mo-Fe_3O_4, respectively) anodes at 100 mA g^{-1} are displayed in **Figure 3a**. Unlike the typical conversion reactions observed in LIBs,[17] the sloping profiles with

drastic capacity suggest much lower electrochemical reactivity due to the sluggish Na^+ kinetics in SIBs.[26] However, the Mo-substituted samples show significant improvements in capacity and voltage hysteresis with increased Mo dopants. The initial discharging capacity for undoped Fe_3O_4 anode is 129.3 mAh g^{-1}, which increases to 188.3, 229.6, 259.2, and 283.1 mAh g^{-1} for 005Mo-Fe_3O_4, 010Mo-Fe_3O_4, 015Mo-Fe_3O_4 and 020Mo-Fe_3O_4 anodes, respectively. Notably, the 020Mo-Fe_3O_4 anode delivers a two-fold capacity increase, mainly originating from the initial intercalation process above 1.0 V vs. Na^+/Na, suggesting that Fe vacancies could serve as available storage sites for the Na^+ intercalation.

Cyclic voltammetry (CV) curves in Figure 3b further elucidate the differences in Na^+ storage. In contrast to the Fe_3O_4 anode, the first cathodic scan for the 020Mo-Fe_3O_4 anode reveals a sloping region from open circuit potential (OCV) to 1.5 V, further testifies the vacancy-mediated Na^+ storage process observed in the discharging profile. Then a distinct peak at ≈1.2 V is ascribed to Na^+ effectively intercalating into 020Mo-Fe_3O_4 lattice with the formation of $Na_xFe_3O_4$ intermediate, discussed below. Additionally, a peak at 0.6 V demonstrates the further reduction of active Fe^{2+}/Fe^{3+} centers and forming the solid electrolyte interface (SEI).[14a] Reversely, two peaks at 0.75 and 1.5 V in the anodic scan are indicative of the reversible oxidation of Fe^{2+}/Fe^{3+} during Na^+ extraction. In the subsequent cycles, the two intensive reduction peaks observed in the first cycle merge into a weaker
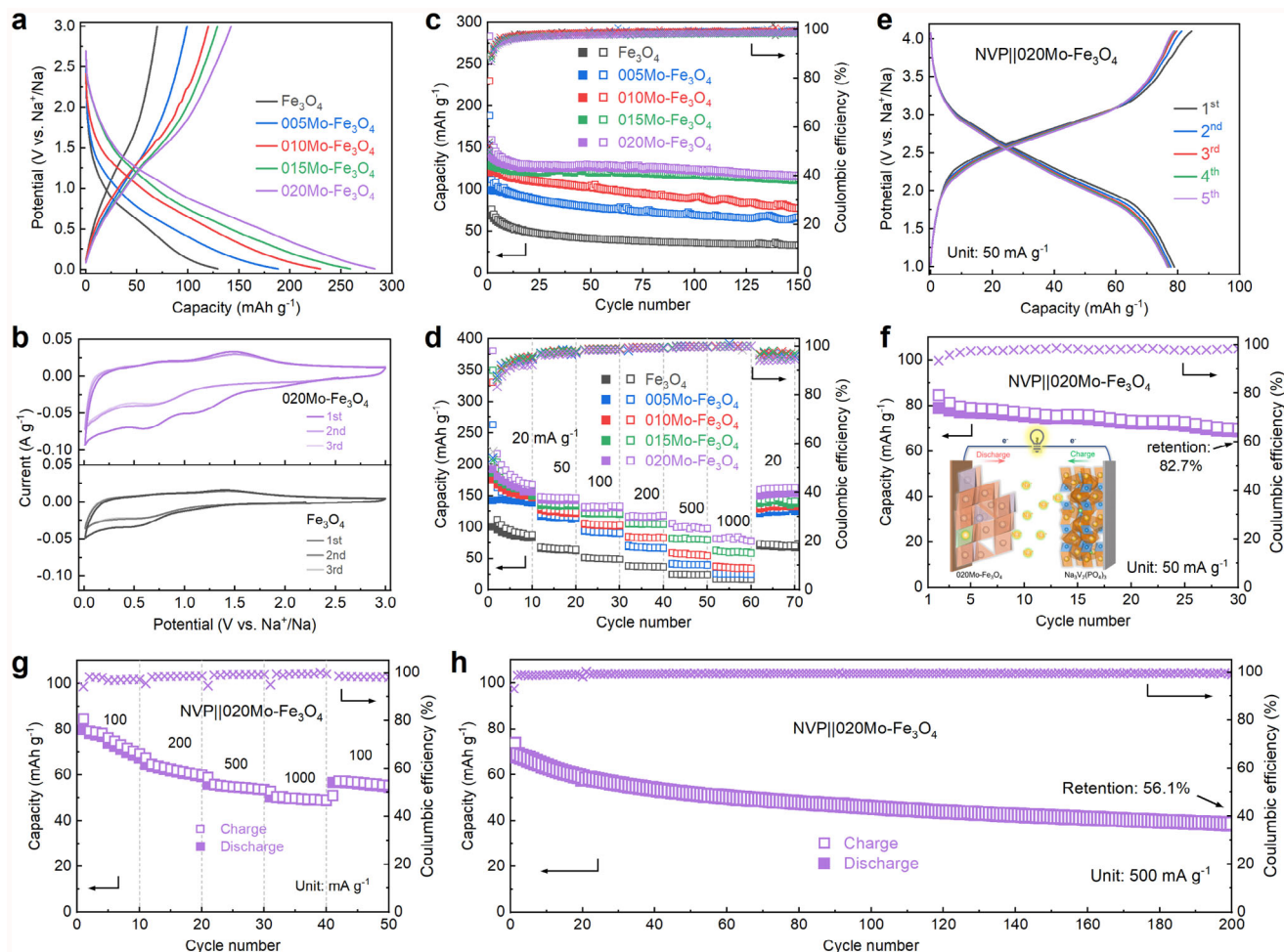
**ADVANCED
SCIENCE NEWS**

www.advancedsciencenews.com

NANO · MICRO

small

www.small-journal.com

Figure 3. Electrochemical performance. a) The initial discharge/charge profiles at galvanostatic 100 mA g^{-1}. b) The first three CV scans at 0.1 mV s^{-1} for 020Mo- Fe$_3$O$_4$ and Fe$_3$O$_4$ electrodes. c) Cycling performance at 100 mA g^{-1}, and d) rate capability of the half cells. The NVP||020Mo-Fe$_3$O$_4$ full cell's e) galvanostatic charging/discharging curves, f) cycling performance at 50 mA g^{-1}, g) rate capability, and h) cycling performance at 500 mA g^{-1}.

one ≈0.78 V, reflecting the irreversible reaction process related to the conversion reaction and SEI formation.[27] The overlapping profiles in the following cycles suggest a stable and reversible sodiation/desodiation process after the initial activation.[28] In the meantime, Mo incorporation also reduces the voltage gap during the first and following cycles, thus reducing the polarization.[29]

The cycling performance in Figure 3c shows the improved stability for Mo-doped samples compared with undoped Fe$_3$O$_4$. The capacities obtained after 150 cycles are ≈32.7, ≈66.8, ≈77.3, ≈112.9, and ≈116.6 mAh g^{-1} with capacity retentions of ≈48.2%, ≈67.4%, ≈61.4%, ≈83.4%, and ≈86.7% for Fe$_3$O$_4$, 005Mo-Fe$_3$O$_4$, 010Mo-Fe$_3$O$_4$, 015Mo-Fe$_3$O$_4$ and 020Mo-Fe$_3$O$_4$, respectively, after the first cycle of activation. We further compare the discharging/charging curves after 10 and 150 cycles, as shown in Figure S4 (Supporting Information). It is observed that the enhanced capacity over cycling is maintained for 020Mo-Fe$_3$O$_4$ anode. Moreover, the rate capability also shows improvements at different current densities, as depicted in Figure 3d. Notably, the 020Mo-Fe$_3$O$_4$ anode achieves reversible capacities of ≈168.0, ≈146.7, ≈133.0, ≈118.4, ≈98.0, and ≈77.7 mAh g^{-1} at current rates of 20, 50, 100, 200, 500 and 1000 mA g^{-1}, respectively. A high capac-

ity of ≈162.5 mAh g^{-1} is recovered when the current returns to 20 mA g^{-1}, indicating excellent rate capability. Considering there are few reports on the deployment of cationic vacancies to modulate atomic/electronic properties of Fe$_3$O$_4$ for unlocking Na intercalation, the activated reversible capacity presented in the 020Mo-Fe$_3$O$_4$ anode is highly encouraging, a comparable table of the electrochemical performance with previous iron-based oxides in SIBs are provided in Table S4 (Supporting Information).

The activated electrochemical performance in Na half cells encourages us to further evaluate the practical application potential of the economical 020Mo-Fe$_3$O$_4$ anode in full cells. The configuration of full cell is elucidated as the inset in Figure 3f, comprised of a NASICON-type Na$_3$V$_2$(PO$_4$)$_3$ (NVP) cathode (Figure S5, Supporting Information) and 020Mo-Fe$_3$O$_4$ anode, denoted as NVP||020Mo-Fe$_3$O$_4$. In Figure 3e, the charging/discharging profiles show a long slope with an average operating voltage of ~2.3 V and an initial capacity of 91.84/71.4 mAh g^{-1}. The Coulombic efficiency is 77.7% initially but increases and maintains over 98% upon cycling (Figure 3f). Figure 3g illustrates the promising rate capability, in which a capacity of 67.3 mAh g^{-1} is obtained at 100 mA g^{-1}, and even at a higher density of 1000 mA g^{-1},
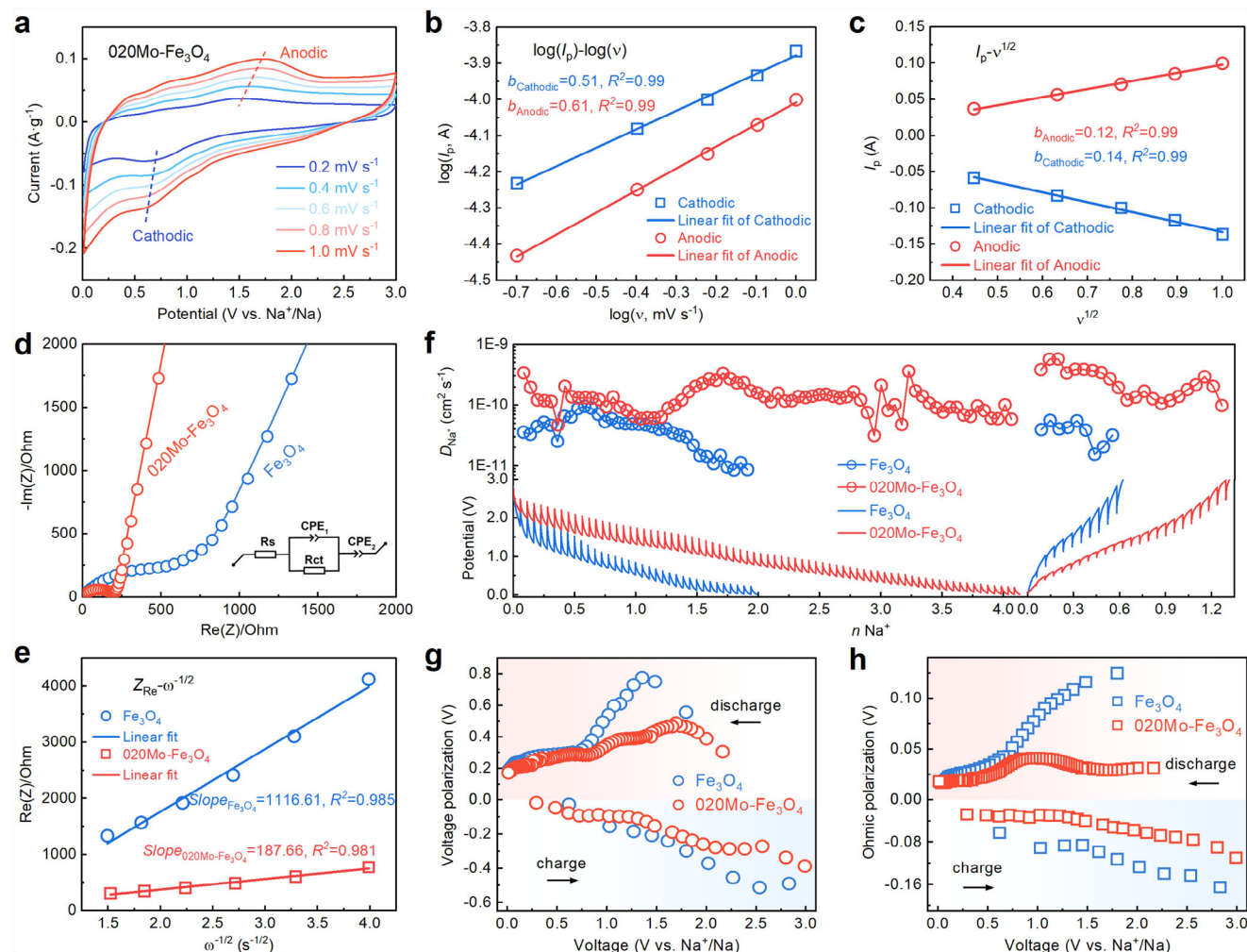
Figure 4. Kinetic analysis. a) CV curves at scanning rates from 0.2 to 1.0 mV s⁻¹ between the voltages of 0.01 V and 3.0 V vs. Na⁺/Na for the 020Mo-Fe₃O₄ electrode. b) Linear fitting between $\log(I_p)$ and $\log(\nu)$ of the CV redox peaks. c) Linear fitting of I_p versus $\nu^{1/2}$. d) EIS Nyquist plots and fitting profiles based on the inset EEC model of 020Mo-Fe₃O₄ and Fe₃O₄ electrodes. e) Linear plots of low-frequency $Z_{Re} - \omega^{-1/2}$. f) GITT profiles along with the calculated diffusion coefficients, g) voltage, and h) ohmic polarization during the first discharge/charge process for 020Mo-Fe₃O₄ and Fe₃O₄ electrodes.

a reversible capacity of 48.8 mAh g⁻¹ is maintained. At 500 mA g⁻¹, a more stable cycling is delivered with higher Coulombic efficiency (higher than 99%) (Figure 3h). The good cycling stability and rate performance of 020Mo-Fe₃O₄ anode demonstrates its practical application potential.

2.3. Kinetics Analysis

Kinetic analyses combining CV, electrochemical impedance spectroscopy (EIS), and galvanostatic intermittent titration technique (GITT) are presented in **Figure 4**. CV scans with different rates are employed to investigate the Na⁺ diffusion behavior, as shown in Figure 4a and Figure S6a (Supporting Information). The peak currents (I_p) and scan rates (ν) adhere to a power-law function (Equation 1) below:

$$I_p = a\,\nu^b \tag{1}$$

where the b-value differentiates the charge-storage mechanisms.[30] The b-values extracted from the slope of linear fit between $\log(I_p)$ and $\log(\nu)$ are 0.51 and 0.62 in the cathodic process, 0.61 and 0.69 in the anodic process for the 020Mo-Fe₃O₄ and undoped Fe₃O₄ anodes, respectively, as shown in Figure 4b and Figure S6b (Supporting Information). These values indicate that the diffusion-controlled process predominantly contributes to the capacity during both sodiation and desodiation reactions for both Mo-doped and undoped Fe₃O₄ anodes. And, the Randles–Sevcik equation (Equation 2) can be used to quantify the Na⁺ diffusion coefficient (D) via the linear plot of $I_p - \nu^{1/2}$:[31]

$$I_p = 2.69 \times 10^5\, n^{3/2}\, C\, A\, D^{1/2}\, \nu^{1/2} \tag{2}$$

where C (mol cm⁻³) indicates the molar concentration of intercalated Na⁺, A (cm²) is the reaction area, and n represents the number of electron transfers. From the slope of Figure 4c and Figure S6c (Supporting Information), the calculated Na⁺ diffusion coefficient ($D_{Na^+}^{CV}$) of 020Mo-Fe₃O₄ anode is

ADVANCED
SCIENCE NEWS

www.advancedsciencenews.com

NANO · MICRO

small

www.small-journal.com

$\approx 4.56 \times 10^{-10}$ cm^2 s^{-1}, showing faster diffusion compared with undoped Fe$_3$O$_4$ ($\approx 1.27 \times 10^{-10}$ cm^2 s^{-1}), testifying the fast bulk sodiation facilitated by Fe vacancies in 020Mo-Fe$_3$O$_4$.

In Figure 4d, EIS Nyquist plots are collected under the OCV state, consisting of two regions: the semicircle representing charge-transfer resistance at high frequency and the linear slope corresponding to Na$^+$ diffusivity within the electrode at low frequency. According to an equivalent electrical circuit model (inset in Figure 4d), the charge-transfer resistances (R_{ct}) are refined to be $\approx 200\,\Omega$ for 020Mo-Fe$_3$O$_4$ and $\approx 760\,\Omega$ for Fe$_3$O$_4$ (Table S5, Supporting Information), demonstrating a higher electronic conductivity after Mo doping.[32] According to the Warburg coefficient (σ_ω) obtained from the linearly fitted Z_{Re} vs. $\omega^{-1/2}$ (Figure 4e), the EIS-based diffusion coefficient is calculated to be $\approx 3.94 \times 10^{-11}$ cm^2 s^{-1} for 020Mo-Fe$_3$O$_4$ higher than $\approx 1.11 \times 10^{-11}$ cm^2 s^{-1} for Fe$_3$O$_4$ (Equation 3 and 4). The increased order in diffusion coincides with the CV analysis, confirming the pivotal role of the defective structure after Mo^{4+}-doping for enhancing diffusion kinetics. Moreover, the critically enhanced diffusion continues over cycling, as confirmed by the EIS Nyquist plots after 10 and 150 cycles in Figure S7 (Supporting Information). The decreased R_{ct} indicates a fast charge transfer between the electrolyte-electrode interface, and the much lower σ_ω indicates a fast kinetic of Na$^+$ within 020Mo-Fe$_3$O$_4$ anode.

$$Z_{Re} = R_s + R_{ct} + \sigma_\omega \omega^{-1/2} \tag{3}$$

$$D = R^2 T^2 / 2A^2 F^4 C^2 \sigma_\omega^{\ 2} \tag{4}$$

Furthermore, GITT is performed to monitor the real-time diffusion of Na$^+$ during the first sodiation/desodiation. The titration curves (Figure 4f) and the Na$^+$ diffusion coefficients, deduced from Equation 5, are plotted as a function of the intercalated Na$^+$ concentration.[33]

$$D_{Na^+}^{GITT} = \frac{4}{\pi} \left(\frac{iV_m}{Z_A FS} \right)^2 \left[\left(\frac{dE}{dx} \right) \Big/ \left(\frac{dE}{d\sqrt{t}} \right) \right]^2 \left(t << \frac{L^2}{D} \right) \tag{5}$$

where dE/dx (V mol^{-1}) indicates the change in voltage to Na$^+$ concentration from the coulometric titration curve, $dE/d\sqrt{t}$ is a linear relation of the potential E (V) against current-pulse duration t (s), Z_A denotes the charge of Na$^+$, V_m (cm^3 mol^{-1}) refers to the molar volume of an electrode, S (cm^2) is electrode-electrolyte contact area, i (A) is the applied current, L (cm) indicates the diffusion length, and F is 96485 C mol^{-1}. Accordingly, the diffusion coefficients calculated in Figure 4f, are 10^{-9} to 10^{-11} cm^2 s^{-1} for 020Mo-Fe$_3$O$_4$ and 10^{-10} to 10^{-12} cm^2 s^{-1} for Fe$_3$O$_4$. Additionally, the 020Mo-Fe$_3$O$_4$ electrode effectively reduces the voltage and ohmic polarization during the discharge/charge process (Figure 4g,h). Even after 150 cycles, the Na$^+$ diffusion within 020Mo-Fe$_3$O$_4$ anode remains relatively stable and much higher than that of Fe$_3$O$_4$ (Figure S8, Supporting Information). These findings reveal that Fe vacancies significantly enhance the Na$^+$ diffusion and suppress the polarization, which are beneficial for achieving excellent cycling performance and rate capability.

3. Discussion

3.1. DFT Calculations

DFT calculations are conducted to gain atomic-level insights into the improved performance of 020Mo-Fe$_3$O$_4$ anode, focusing on Na$^+$ intercalation behavior, including the intercalation energies, density of states (DOS), and migration barriers. As shown in **Figure 5a**, the induced Fe vacancies in the 020Mo-Fe$_3$O$_4$ anode present a more readily intercalation energy for Na$^+$ at the Fe vacancy sites of (-3.003 eV) compared to the interstitial sites of Fe$_3$O$_4$ anode (-0.033 eV). This indicates that Fe vacancies offer reactive sites for Na$^+$ intercalation due to the enhanced bonding and chemical interactions between Na$^+$ and defective anode.[34] For a more detailed analysis, the calculated DOS in Figure 5b illustrates the electronic structure modification induced by the Mo doping and Na$^+$ intercalation. The Mo incorporation creates interactions between Mo and O atoms, altering the total hybridizations of metal and oxygen ions, which leads to a reduced bandgap and ameliorated electronic conductivity.[35] Moreover, the Mo-O hybridization is also favorable for sodiation with the declined interactions between the intercalated Na$^+$ and O^{2-}, which is further evidenced by the DOS after Na$^+$ intercalation.[36] Specifically, in defect-free Fe$_3$O$_4$ anode, the high electrostatic repulsion of Na$^+$ at the interstitial sites causes strong perturbations to the electronic structure, contributing to the arising of Fe-orbitals at the valence band maximum. In contrast, the defective 020Mo-Fe$_3$O$_4$ anode shows that Na$^+$ intercalation at the vacancy sites improves the electronic density near the Fermi level. Notably, the valence band maximum and conduction band minimum shift toward the Fermi level, producing a narrow bandgap. This effect is especially pronounced when Na$^+$ is located at the vacancy sites, where new states occur at the Fermi level, reflecting the enhanced electronic conductivity.[37]

The Na$^+$ diffusion behaviors in the defective and defect-free anodes were further predicted to explore migration paths and corresponding energy barriers using the nudged elastic band method (Figure 5c,d). In the defect-free Fe$_3$O$_4$ anode (blue region), Na$^+$ migrates between the octahedral interstitial sites, encountering strong electrostatic repulsion from neighboring cations,[38] resulting in a high energy barrier of 4.11 eV. In contrast, the cation-deficient 020Mo-Fe$_3$O$_4$ anode features low-energy vacancies that facilitate Na$^+$ migration along vacancy-mediated paths and provide active sites for Na$^+$ intercalation, significantly reducing the energy barrier to 0.42 eV. These observations suggest that the defective 020Mo-Fe$_3$O$_4$ structure, tailored by Mo^{4+} doping, not only narrows the bandgap and improves electronic conductivity, but also creates a less restrictive Coulombic repulsion channel, leading to the low-barrier and vacancy-mediated migration paths,[17,39] thus accelerating Na$^+$ diffusion to ensure the fast Na$^+$ intercalation and excellent rate capability achieved.

3.2. Structural Evolutions

Operando XRD is employed to monitor the real-time structural transformation during the initial three sodiation and desodiation cycles. The 2D contour plots and corresponding lattice parameters for the 020Mo-Fe$_3$O$_4$ and pristine Fe$_3$O$_4$ electrodes are
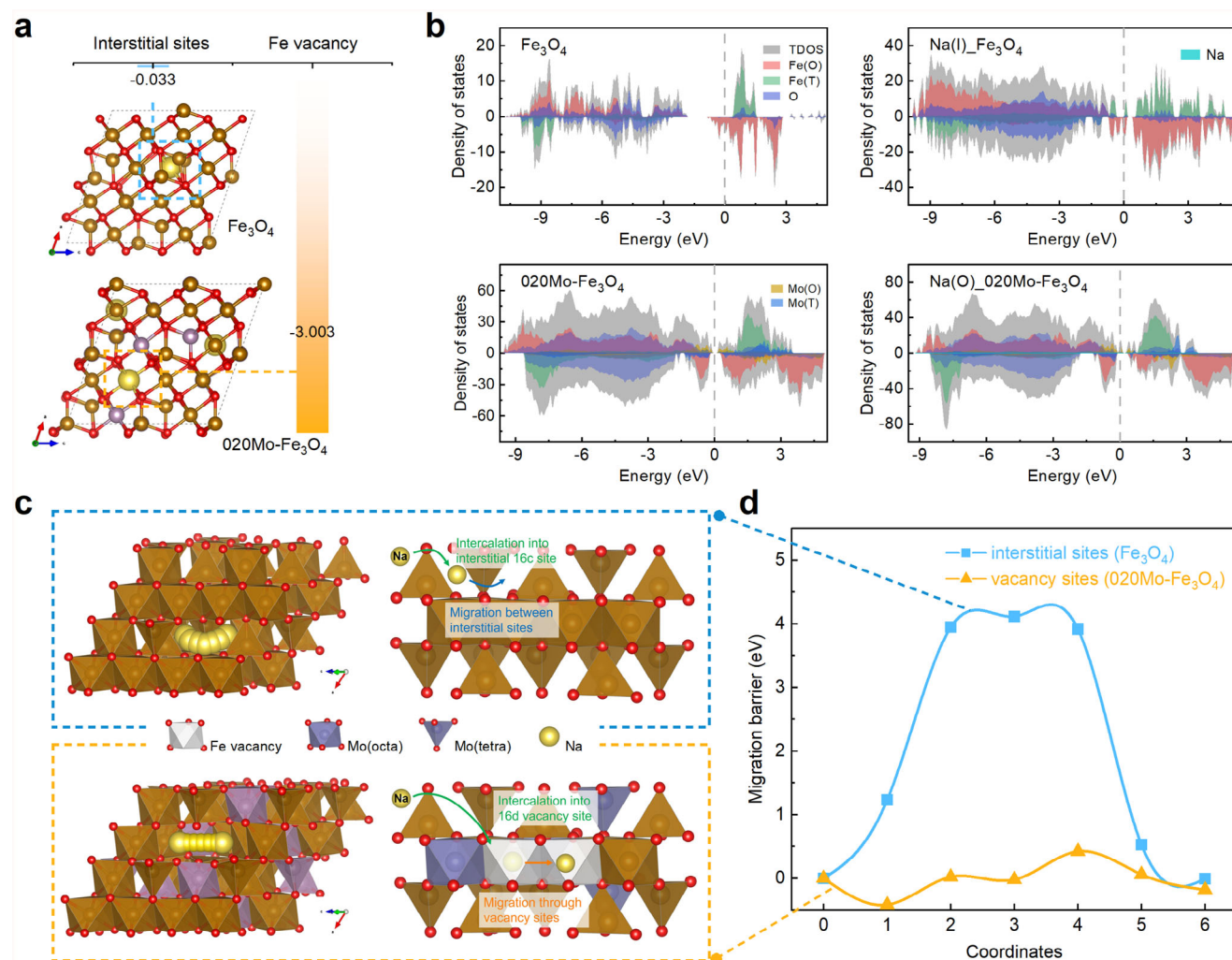
Figure 5. DFT calculations. a) Intercalation energy of Na^+ at the Fe vacancy sites inside the 020Mo-Fe_3O_4 anode (orange) compared to the interstitial sites in the Fe_3O_4 anode (blue). b) Density of states before and after Na^+ intercalation into the interstitial sites in Fe_3O_4 (Na(I)_Fe_3O_4) and the vacancy sites in 020Mo-Fe_3O_4 (Na(O)_020Mo-Fe_3O_4). c) Schematics of migration pathways and d) the corresponding energy barriers of Na^+ migrates through the interstitial sites in defect-free Fe_3O_4 (blue) and migrates through the vacancy sites in the defective 020Mo-Fe_3O_4 (orange).

illustrated in **Figure 6**. Complementary ex situ XRD with Rietveld refinements is conducted to further elucidate structural evolution and intercalated sodium occupancy (Figure S9 and S10, Supporting Information). For Fe_3O_4 anode, the negligible changes in the intensity and position of diffraction peaks are observed, as shown in Figure 6b. The refined ex situ XRD further delivers that only 0.15 Na^+ intercalates into the interstitial 16c sites at the initial discharging region (OCV – 1.0 V) (Figure S9, Supporting Information), which is responsible for the negligible impact on the crystal structure. While for the 020Mo-Fe_3O_4 anode, it is obvious that both positions and intensities of (220), (311), and (400) peaks change during the initial cycling, as shown in Figure 6a. From OCV to 1.0 V, the three peaks shift to lower angles, indicating an intercalation-dominant process where Na^+ occupies the available active sites. The refined ex situ XRD pattern at 1.0 V suggests that ≈0.66 Na^+ intercalation (Figure S10, Supporting Information), further evidencing the vacancy-mediated intercalation mechanism, in good line with the DFT calculations.

As the sodiation proceeds, strong electrostatic repulsion between the intercalated Na^+ and Fe ions induces cation rearrangements, with Fe^{3+} transforming from 8a to 16c sites, which is responsible for the weakened reflections of the (220) peak.[13a,40] Significantly, new diffraction peaks at 36.8° and 42.5° indexed to the $Na_xFe_3O_4$ phase occurs at ≈0.8 V, equivalent to 1-electron transfer.[41] The transformation from the original 020Mo-Fe_3O_4 to the $Na_xFe_3O_4$ phase continues until the end of sodiation. During charging, the reflections of (220), (311), and (400) for 020Mo-Fe_3O_4 are partially recovered and shift to higher angles, indicating an irreversible reaction process that is responsible for the low initial Coulombic efficiency.[42] Unlike the conversion reaction observed with the disappearance of the initial phase at the end of discharge in LIBs,[17] Na^+ intercalation in 020Mo-Fe_3O_4 follows a partial conversion process with the reversible structure evolution of $Na_xFe_3O_4$ intermediate and 020Mo-Fe_3O_4 initial phase (Figure S11a,b, Supporting Information).[41] Even after 150 cycles, the 020Mo-Fe_3O_4 initial phase is also preserved, with lattice

**ADVANCED
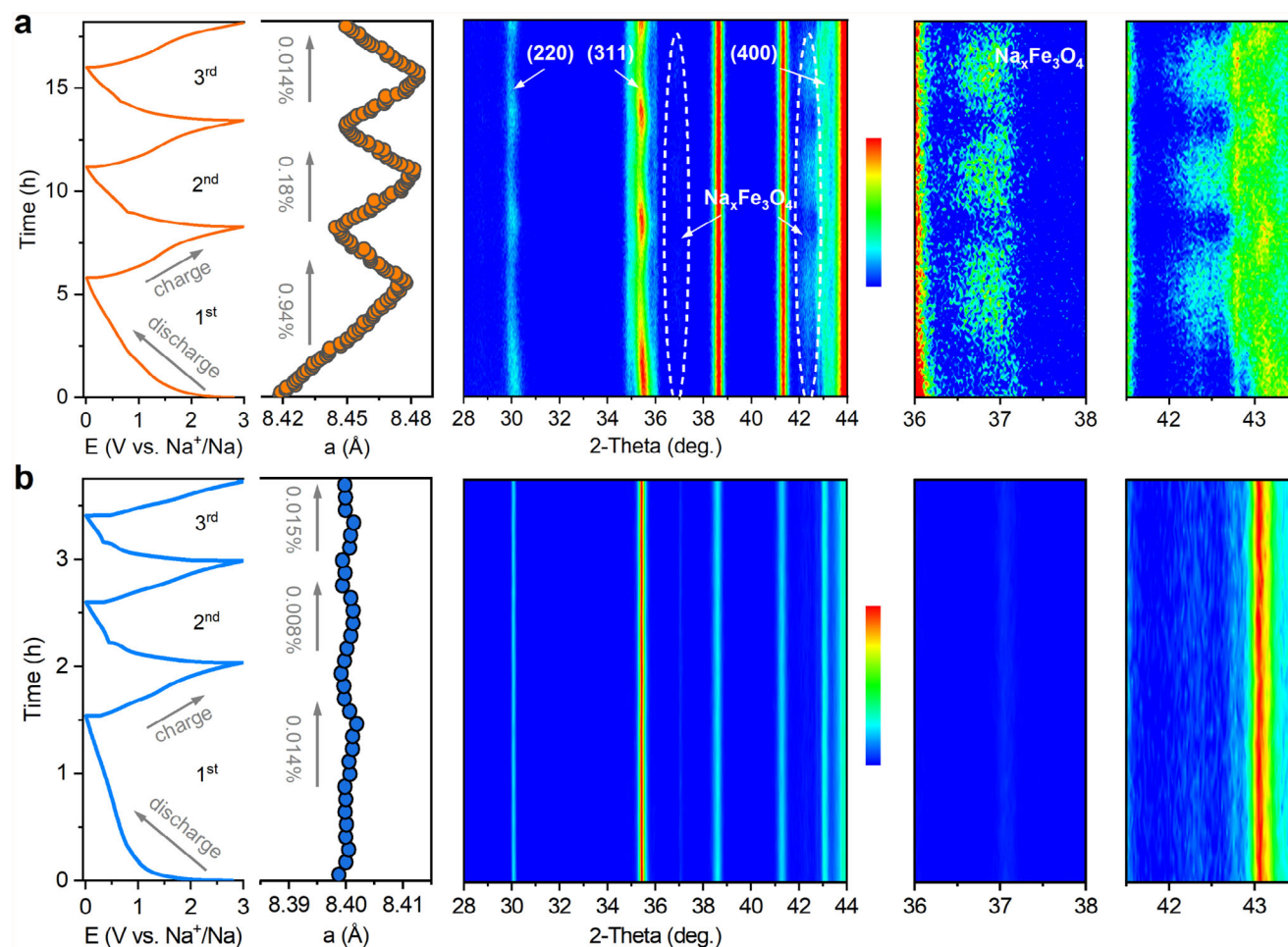SCIENCE NEWS**

www.advancedsciencenews.com

NANO · MICRO

small

www.small-journal.com

Figure 6. Operando XRD patterns of the a) 020Mo-Fe_3O_4 anode and b) Fe_3O_4 anode. The galvanostatic profiles at 50mA g^{-1}, refined lattice parameters, 2D contour plots, and magnified regions are illustrated from left to right.

expansion and grain reduction originating from the effective Na^+ intercalation, as shown by the XRD and selected area electron diffraction (SAED) patterns in Figure S11c,d (Supporting Information).

To further elucidate the Na^+ storage mechanism, variations in electronic properties at different depths of discharge and states of charge are examined. Fe $L_{2,3}$ edge XAS provides fingerprints of Fe $3d$ orbitals, which is closely related to the electrochemical process.[43] In Figure S12 (Supporting Information), Fe L_3 and L_2 peaks shift toward lower absorption energy as the system transitions from Fe^{3+}-dominance at OCV to Fe^{2+}-dominance at 0.01 V, indicating the reduction of Fe^{3+}/Fe^{2+} centers during the sodiation. However, these peaks do not revert to their original state upon charging to 3.0 V, reflecting the irreversible process detected by XRD. In contrast, the Fe $L_{2,3}$ edge XAS of Fe_3O_4 anode shows negligible changes (Figure S13, Supporting Information), further verifying the limited sodiation.

4. Conclusion

In summary, by the rational design of cation-deficient Fe_3O_4 through the foreign Mo^{4+} doping, we deploy a defective Fe_3O_4

as a potential anode for SIBs. The defective anode significantly activates sodium storage within the spinel structure, demonstrating excellent cycling performance and rate capability. Comprehensive structural analyses, including PDF modeling, XRD refinements, and XAS, confirm that Mo^{4+} is uniformly integrated into the Fe_3O_4 framework at both tetrahedral and octahedral sites, introducing and stabilizing more Fe vacancies in the meantime. This defective 020Mo-Fe_3O_4 anode delivers an improved Na^+ storage performance. The capacity retention increases from ≈48.2% to ≈86.7% at 100 mA g^{-1} after 150 cycles, and the rate capability is remarkably enhanced compared with defect-free Fe_3O_4. Kinetic analysis reveals the enhanced charge transfer and a twofold increase of Na^+ diffusion coefficient. DFT calculations show the modulated atomic and electronic properties induced by the Mo dopant, narrowing the bandgap with promoted electronic conductivity. And, the charge-compensated Fe vacancies serve as active storage sites and direct a low-energy barrier pathway to accelerate Na^+ diffusion within the bulk structure. This study offers a novel insight for designing the defective structure in TMOs to activate fast and reversible Na^+ intercalation, thus developing high-performance anodes for advanced SIBs.

Supporting Information

Supporting Information is available from the Wiley Online Library or from the author.

Acknowledgements

Conflict of Interest

The authors declare no conflict of interest.

Data Availability Statement

The data that support the findings of this study are available from the corresponding author upon reasonable request.

Keywords

[1] W. Guo, T. Feng, W. Li, L. Hua, Z. Meng, K. Li, *J. Energy Storage* **2023**, *72*, 108589.

[2] a) S.-W. Kim, D.-H. Seo, X. Ma, G. Ceder, K. Kang, *Adv. Energy Mater.* **2012**, *2*, 710; b) C. Vaalma, D. Buchholz, M. Weil, S. Passerini, *Nat. Rev. Mater.* **2018**, *3*, 18013; c) P. K. Nayak, L. Yang, W. Brehm, P. Adelhelm, *Angew. Chem., Int. Ed.* **2018**, *57*, 102.

[3] J.-Y. Hwang, S.-T. Myung, Y.-K. Sun, *Chem. Soc. Rev.* **2017**, *46*, 3529.

[4] M. Valvo, F. Lindgren, U. Lafont, F. Björefors, K. Edström, *J. Power Sources* **2014**, *245*, 967.

[5] a) H. Pan, Y.-S. Hu, L. Chen, *Energy Environ. Sci.* **2013**, *6*, 2338; b) Y. Sun, S. Guo, H. Zhou, *Adv. Energy Mater.* **2019**, *9*, 1800212.

[6] a) D. Kundu, E. Talaie, V. Duffort, L. F. Nazar, *Angew. Chem., Int. Ed.* **2015**, *54*, 3431; b) H. Zhang, Y. Gao, X. Liu, L. Zhou, J. Li, Y. Xiao, J. Peng, J. Wang, S.-L. Chou, *Adv. Energy Mater.* **2023**, *13*, 2300149.

[7] Y. Kim, K.-H. Ha, S. M. Oh, K. T. Lee, *Chem. - Eur. J.* **2014**, *20*, 11980.

[8] P. Ge, M. Fouletier, *Solid State Ionics* **1988**, *28–30*, 1172.

[9] X.-P. Yin, Y.-F. Zhao, Y.-J. Zhang, *J. Electrochem.* **2023**, *29*, 2204301.

[10] a) L. Zhang, W. Wang, S. Lu, Y. Xiang, *Adv. Energy Mater.* **2021**, *11*, 2003640; b) T. Zhang, C. Li, F. Wang, A. Noori, M. F. Mousavi, X. Xia, Y. Zhang, *Chem. Rec.* **2022**, *22*, 202200083.

[11] a) P. Poizot, S. Laruelle, S. Grugeon, L. Dupont, J. M. Tarascon, *Nature* **2000**, *407*, 496; b) J. Cabana, L. Monconduit, D. Larcher, M. R. Palacín, *Adv. Mater.* **2010**, *22*, E170; c) S. Fang, D. Bresser, S. Passerini, *Adv. Energy Mater.* **2020**, *10*, 1902485.

[12] a) K. He, S. Zhang, J. Li, X. Yu, Q. Meng, Y. Zhu, E. Hu, K. Sun, H. Yun, X.-Q. Yang, Y. Zhu, H. Gan, Y. Mo, E. A. Stach, C. B. Murray, D. Su, *Nat. Commun.* **2016**, *7*, 11441; b) W. Zhang, D. C. Bock, C. J. Pelliccione, Y. Li, L. Wu, Y. Zhu, A. C. Marschilok, E. S. Takeuchi, K. J. Takeuchi, F. Wang, *Adv. Energy Mater.* **2016**, *6*, 1502471.

[13] a) M. A. Islam, J. Bouldin, J. Yang, S.-D. Han, *ACS Appl. Mater. Interfaces* **2022**, *14*, 50773; b) L. Li, Y. Zheng, S. Zhang, J. Yang, Z. Shao, Z. Guo, *Energy Environ. Sci.* **2018**, *11*, 2310.

[14] a) J. Ni, M. Sun, L. Li, *Adv. Mater.* **2019**, *31*, 1902603; b) N. Zhang, X. Han, Y. Liu, X. Hu, Q. Zhao, J. Chen, *Adv. Energy Mater.* **2015**, *5*, 1401123; c) L.-Y. Qi, Y.-W. Zhang, Z.-C. Zuo, Y.-L. Xin, C.-K. Yang, B. Wu, X.-X. Zhang, H.-H. Zhou, *J. Mater. Chem. A* **2016**, *4*, 8822.

[15] a) B. P. Hahn, J. W. Long, D. R. Rolison, *Acc. Chem. Res.* **2013**, *46*, 1181; b) S. I. Ahmed, Z. K. Heiba, N. Y. Mostafa, A. A. Shaltout, H. S. Aljoudy, *Ceram. Int.* **2018**, *44*, 20692; c) B. P. Hahn, J. W. Long, A. N. Mansour, K. A. Pettigrew, M. S. Osofsky, D. R. Rolison, *Energy Environ. Sci.* **2011**, *4*, 1495; d) J. Gao, X. Yan, C. Huang, Z. Zhang, X. Fu, Q. Chang, F. He, M. Li, Y. Li, *Angew. Chem., Int. Ed.* **2023**, *62*, 202307874.

[16] P. Gao, Z. Chen, Y. Gong, R. Zhang, H. Liu, P. Tang, X. Chen, S. Passerini, J. Liu, *Adv. Energy Mater.* **2020**, *10*, 1903780.

[17] S. Guo, T. Koketsu, Z. Hu, J. Zhou, C.-Y. Kuo, H.-J. Lin, C.-T. Chen, P. Strasser, L. Sui, Y. Xie, J. Ma, *Small* **2022**, *18*, 2203835.

[18] a) T. Egami, S. J. L. Billinge, in *Pergamon Materials Series*, *16*, Elsevier, Amsterdam, The Netherlands **2012**, 2; b) S. J. L. Billinge, S. H. Skjaervoe, M. W. Terban, S. Tao, L. Yang, Y. Rakita, B. A. Frandsen, *Molecular Sciences and Chemical Engineering*, Elsevier, Amsterdam, The Netherlands **2021**.

[19] a) J. Zhao, X. Wang, X. Shen, C. J. Sahle, C. Dong, H. Hojo, Y. Sakai, J. Zhang, W. Li, L. Duan, T.-S. Chan, C.-T. Chen, J. Falke, C.-E. Liu, C.-Y. Kuo, Z. Deng, X. Wang, R. Yu, R. Yu, Z. Hu, M. Greenblatt, C. Jin, *Chem. Mater.* **2022**, *34*, 97; b) Y. Ji, H. Wang, X. Li, Y. Meng, Y. Wang, X. Ye, Z. Liu, L. Wang, J. Yang, Q. Guo, H. Zhuang, X. Shen, C.-W. Kao, T.-S. Chan, Z. Hu, H. Yang, Y. Long, R. Yu, *J. Solid State Chem.* **2023**, *327*, 124285.

[20] a) N. Hollmann, Z. Hu, A. Maignan, A. Günther, L. Y. Jang, A. Tanaka, H. J. Lin, C. T. Chen, P. Thalmeier, L. H. Tjeng, *Phys. Rev. B* **2013**, *87*, 155122; b) S. C. Liao, S. C. Haw, C. Y. Kuo, H. Guo, H. B. Vasili, S. M. Valvidares, A. C. Komarek, H. Ishii, S. A. Chen, H. J. Lin, A. Tanaka, T. S. Chan, L. H. Tjeng, C. T. Chen, Z. Hu, J. M. Chen, *Phys. Rev. B* **2019**, *99*, 075110.

[21] H. Deng, M. Liu, M. Valldor, Z. Hu, C. Kuo, Y. Yin, J. Yang, X. Wang, Q. Zhao, Y. Xu, Z. Fu, J. Cai, H. Guo, K. Jin, T. Pi, Y. Soo, G. Zhou, J. Cheng, K. Chen, P. Ohresser, Y.-f. Yang, C. Jin, L.-H. Tjeng, Y. Long, *Phys. Rev. B* **2016**, *94*, 024414.

[22] a) N. Hollmann, Z. Hu, M. Valldor, A. Maignan, A. Tanaka, H. H. Hsieh, H. J. Lin, C. T. Chen, L. H. Tjeng, *Phys. Rev. B* **2009**, *80*, 085111; b) N. Hollmann, M. Valldor, H. Wu, Z. Hu, N. Qureshi, T. Willers, Y. Y. Chin, J. C. Cezar, A. Tanaka, N. B. Brookes, L. H. Tjeng, *Phys. Rev. B* **2011**, *83*, 180405.

[23] T. Burnus, Z. Hu, H. Wu, J. C. Cezar, S. Niitaka, H. Takagi, C. F. Chang, N. B. Brookes, H. J. Lin, L. Y. Jang, A. Tanaka, K. S. Liang, C. T. Chen, L. H. Tjeng, *Phys. Rev. B* **2008**, *77*, 205111;

[24] C. F. Chang, Z. Hu, S. Klein, X. H. Liu, R. Sutarto, A. Tanaka, J. C. Cezar, N. B. Brookes, H. J. Lin, H. H. Hsieh, C. T. Chen, A. D. Rata, L. H. Tjeng, *Phys. Rev. X* **2016**, *6*, 041011.

[25] X. Zheng, S. S. Mofarah, C. Cazorla, R. Daiyan, A. A. Esmailpour, J. Scott, Y. Yao, S. Lim, V. Wong, E. Y. Chen, H. Arandiyan, P. Koshy, C. C. Sorrell, *Adv. Funct. Mater.* **2021**, *31*, 2103171.

[26] M. Yu, L. Sun, X. Ning, *J. Alloys Compd.* **2021**, *878*, 160359.

[27] Y. Zhao, F. Wang, C. Wang, S. Wang, C. Wang, Z. Zhao, L. Duan, Y. Liu, Y. Wu, W. Li, D. Zhao, *Nano Energy* **2019**, *56*, 426.

[28] Y. Zhou, W. Sun, X. Rui, Y. Zhou, W. J. Ng, Q. Yan, E. Fong, *Nano Energy* **2016**, *21*, 71.

[29] H. T Huu, N. H. Vu, H. Ha, J. Moon, H. Y. Kim, W. B. Im, *Nat. Commun.* **2021**, *12*, 3081.

[30] a) L. Zhang, X. Zhang, G. Tian, Q. Zhang, M. Knapp, H. Ehrenberg, G. Chen, Z. Shen, G. Yang, L. Gu, F. Du, *Nat. Commun.* **2020**, *11*, 3490; b) S. Niu, R. McFeron, F. Godínez-Salomón, B. S. Chapman, C. A. Damin, J. B. Tracy, V. Augustyn, C. P. Rhodes, *Chem. Mater.* **2017**, *29*, 7794; c) H. Wan, G. Liu, Y. Li, W. Weng, J. P. Mwizerwa, Z. Tian, L. Chen, X. Yao, *ACS Nano* **2019**, *13*, 9551; d) C. Choi, D. S. Ashby, D. M. Butts, R. H. Deblock, Q. Wei, J. Lau, B. Dunn, *Nat. Rev. Mater.* **2019**, *5*, 5.

[31] a) L. P. Wang, X. D. Zhang, T. S. Wang, Y. X. Yin, J. L. Shi, C. R. Wang, Y. G. Guo, *Adv. Energy Mater.* **2018**, *8*, 1801528; b) R. Wang, X. Chen, Z. Huang, J. Yang, F. Liu, M. Chu, T. Liu, C. Wang, W. Zhu, S. Li, S. Li, J. Zheng, J. Chen, L. He, L. Jin, F. Pan, Y. Xiao, *Nat. Commun.* **2021**, *12*, 3085.

[32] Q. Wang, C. Tang, D. Sun, A. Du, J. Z. Ou, M. Wu, H. Zhang, *Chem. Eng. J.* **2022**, *427*, 131652.

[33] J. Hou, M. Hadouchi, L. Sui, J. Liu, M. Tang, W. H. Kan, M. Avdeev, G. Zhong, Y.-K. Liao, Y.-H. Lai, Y.-H. Chu, H.-J. Lin, C.-T. Chen, Z. Hu, Y. Huang, J. Ma, *Energy Storage Mater.* **2021**, *42*, 307.

[34] M. Gu, A. M. Rao, J. Zhou, B. Lu, *Chem. Sci.* **2024**, *15*, 2323.

[35] Y. Ma, M. Xu, R. Liu, H. Xiao, Y. Liu, X. Wang, Y. Huang, G. Yuan, *Energy Storage Mater.* **2022**, *48*, 212.

[36] J. Yang, J. Wang, X. Dong, L. Zhu, D. Hou, W. Zeng, J. Wang, *Appl. Surf. Sci.* **2021**, *544*, 148775.

[37] S. Li, Y. Liu, X. Zhao, K. Cui, Q. Shen, P. Li, X. Qu, L. Jiao, *Angew. Chem., Int. Ed.* **2021**, *60*, 20286.

[38] C. N. Lininger, C. A. Cama, K. J. Takeuchi, A. C. Marschilok, E. S. Takeuchi, A. C. West, M. S. Hybertsen, *Chem. Mater.* **2018**, *30*, 7922.

[39] a) N. Zhang, F. Cheng, Y. Liu, Q. Zhao, K. Lei, C. Chen, X. Liu, J. Chen, *J. Am. Chem. Soc.* **2016**, *138*, 12894; b) T. Koketsu, J. Ma, B. J. Morgan, M. Body, C. Legein, W. Dachraoui, M. Giannini, A. Demortière, M. Salanne, F. Dardoize, H. Groult, O. J. Borkiewicz, K. W. Chapman, P. Strasser, D. Dambournet, *Nat. Mater.* **2017**, *16*, 1142.

[40] S. Komaba, T. Mikumo, N. Yabuuchi, A. Ogata, H. Yoshida, Y. Yamada, *J. Electrochem. Soc.* **2010**, *157*, A60.

[41] D.-Y. Park, S.-T. Myung, *ACS Appl. Mater. Interfaces* **2014**, *6*, 11749.

[42] H. He, D. Sun, Y. Tang, H. Wang, M. Shao, *Energy Storage Mater.* **2019**, *23*, 233.

[43] J. Shirakawa, M. Nakayama, M. Wakihara, Y. Uchimoto, *J. Phys. Chem. B* **2007**, *111*, 1424.